AIAA JOURNAL
Vol. 40, No. 2, February 2002

Role of Actuation Frequency in Controlled Flow Reattachment over a Stalled Airfoil

Michael Amitay*
Georgia Tech Research Institute, Atlanta, Georgia 30332
and
Ari Glezer†
Georgia Institute of Technology, Atlanta, Georgia 30332-0405

The effect of the actuation frequency on the manipulation of the global aerodynamic forces on lifting surfaces using surface-mounted fluidic actuators based on synthetic (zero mass flux) jet technology is demonstrated in wind-tunnel experiments. The effect of the actuation is investigated at two ranges of (dimensionless) jet formation frequencies of the order of, or well above, the natural shedding frequency. The vortical structures within the separated flow region vary substantially when the dimensionless actuation frequency F^+ is varied between $\mathcal{O}(1)$ and $\mathcal{O}(10)$. When F^+ is $\mathcal{O}(1)$, the reattachment is characterized by the formation of large vortical structures at the driving frequency that persist well beyond the trailing edge of the airfoil. The formation and shedding of these vortices leads to unsteady attachment and, consequently, to a time-periodic variation in vorticity flux and in circulation. Actuation at F^+ of $\mathcal{O}(10)$ leads to a complete flow reattachment that is marked by the absence of organized vortical structures along the flow surface. This suggests that when the actuation frequency is high enough, the Coanda-like attachment of the separated shear layer to the top (suction) surface of the airfoil can be replaced by completely attached flow for which separation may be bypassed altogether.

I. Introduction

CONTROLLED reattachment of separated flows over lifting surfaces at moderate and high angles of attack by means of fluidic actuation, with the objectives of improving aerodynamic performance and extending the flight envelope, has been the subject of numerous investigations since the 1950s. Fluidic actuation has been conceptually divided into two primary disciplines that are characterized by the temporal nature of the actuation. The traditional, time-invariant actuation has been based on continuous suction[1] or blowing[2] and has typically required substantial mass (and momentum) flux to achieve some measure of efficacy. In contrast, a substantial body of work since the early 1980s has demonstrated that, in many cases, temporally variant actuation can effectively replace the continuous actuation and in many cases achieve better results at a fraction of the mass flux.[3]

Flow around an object can also be controlled by mechanical devices such as an oscillating fence[4] and a rotating cylinder.[5] The mechanical devices operate as momentum injectors into the boundary layer. Urzynicok et al.[4] found that this type of mechanical actuation on Wortmann FX 61-184 laminar glider along the entire span yields an increase in lift up to 40%. On the other hand, the rotating cylinder installed on a two-dimensional symmetric airfoil[5] increased maximum lift by as much as 210% and delayed stalled up to 48 deg ($Re_c = 3 \times 10^4$–5×10^5).

Unsteady actuation, which exploited the receptivity of the separating shear layer to external excitation [Ahuja and Burrin[6] (acoustic excitation) and Seifert et al.[3] (steady and unsteady blowing)], had shown that the time-averaged lift can be substantially increased. As a result of the modification of global entrainment by the shear layer, a Coanda-like deflection toward the flow boundary is induced, which leads to partial restoration of lift.

The actuation affecting the separating shear layer was typically applied at a dimensionless frequency $F^+ \sim \mathcal{O}(1)$ ($F^+ = f_{\text{act}} L/U_\infty$, where f_{act} is the actuation frequency, L is a characteristic length of the separated region, and U_∞ is the freestream velocity) having a characteristic period that scales with time of flight over the streamwise length of the affected flow domain.[3] However, the work of Chang et al.[7] demonstrated that lift recovery can be attained over a much broader range of actuation frequencies that far exceed the unstable frequency of the separating shear layer (up to $F^+ = 20$).

More recently, Smith et al.[8] and Amitay et al.[9,10] demonstrated the suppression of separation over an unconventional airfoil (the leading edge of which was an azimuthal section of a circular cylinder mounted within a uniformly stretched NACA four-digit series symmetric airfoil fairing) at moderate Reynolds numbers (up to 10^6, based on the chord and the freestream velocity) that resulted in a dramatic increase in lift and a corresponding decrease in pressure drag. Actuation was effected using synthetic (zero mass flux) jet actuators, which were deliberately operated at frequencies that were typically an order of magnitude higher than the characteristic (shedding) frequency of the airfoil, that is, $F^+ \sim \mathcal{O}(10)$ rather than $F^+ \sim \mathcal{O}(1)$. These authors argued that the interaction of high-frequency zero net mass flux jets with the crossflow leads to local modification of the apparent aerodynamic shape of the flow surface and, as a result, to full or partial suppression of flow separation. Moreover, the recent experiments of Erk[11] demonstrated the suppression of separation on an FX61-184 airfoil at Reynolds numbers up to 3×10^6 using synthetic jet actuation at frequencies up to $F^+ \sim \mathcal{O}(100)$.

The present work builds on the earlier results of Amitay et al.[12] and focuses on the differences in the response of the separated flow to actuation at two distinct frequency bands. The first band includes the unstable frequencies of the separating shear layer, that is, $F^+ \sim \mathcal{O}(1)$, whereas the second frequency band is well above the receptivity range of the shear layer, that is, $F^+ \sim \mathcal{O}(10)$.

II. Experimental Apparatus and Procedures

The experiments are conducted in an open-return low-speed wind tunnel having a square test section measuring 91 cm on a side. The maximum air speed is 32 ± 1 m/s with a freestream turbulence level less than 0.25%. The upper and lower walls of the wind tunnel are adjusted to compensate for blockage created by the airfoil. The airfoil model (Fig. 1) comprises a 62-mm-diam leading-edge circular cylinder mounted within an aerodynamic fairing based on a

Received 5 October 2000; revision received 5 July 2001; accepted for publication 9 August 2001.

*Research Engineer, Aerospace, Transportation, and Advanced Systems Laboratory; michael.amitay@me.gatech.edu. Member AIAA.

†Professor, School of Mechanical Engineering; ari.glezer@me.gatech.edu. Associate Member AIAA.

uniformly stretched NACA four-digit series symmetric airfoil, for which the thickness to chord ratio d/c is 24% ($c = 254$ mm). An important attribute of this configuration is that it allows for continuous variation of the azimuthal position of the jet between −90 and +90 deg (relative to the chord of the airfoil; see Amitay et al.[12]). The surfaces of the cylinder and of the fairing are well polished, and the transition between the surface of the cylinder and the edge of the fairing is designed to have a close fit with minimal surface discontinuity. At a given angle of attack and actuator jet angle, the junction between the cylinder and the fairing is sealed with a thin tape.

The cylinder is instrumented with 47 pressure taps that are located in the spanwise mid-plane and are equally spaced circumferentially around the cylinder. Similarly, the fairing is instrumented with 45 pressure taps along the top and bottom surfaces and at the same spanwise location as the taps on the cylinder. The pressure data are obtained using two 48-channel Scanivalve systems, and a 10-torr Baratron pressure transducer is used to obtain mean pressure data. The resolution of the pressure transducer is 0.001% of full scale of 10 torr. The center section of the leading-edge cylinder also houses a pair of flush-mounted adjacent high aspect ratio rectangular (140 × 0.5 mm) synthetic jet actuators. The long side of each rectangular orifice is collinear with the axis of the cylinder, and the two orifices are 2.5 mm apart azimuthally. High-frequency synthetic jets are produced at $F^+ = 10$, 14.7, and 20 ($f_{act} = 740$, 1088, and 1480 Hz, respectively) using piezoelectrically driven diaphragms mounted in compact shallow cavities underneath the surface of the cylinder. Low-frequency synthetic jets are produced (through the same orifices) at $F^+ = 0.95$, 2.05, and 3.3 ($f_{act} = 71$, 148, and 246 Hz, respectively) by conventional pressure speakers mounted on opposite ends of the cylinder cavity (in the absence of the piezoelectric drivers).

The actuator performance is measured using the momentum coefficient

$$C_\mu = \bar{I}_j \Big/ \tfrac{1}{2}\rho_0 U_0^2 c \tag{1}$$

where $\bar{I}_j$ is the time-averaged momentum flux per unit length during the outstroke and is given by

$$\bar{I}_j = \frac{1}{\tau}\rho_j b \int_0^\tau \left\langle u_j^2(\phi)\right\rangle \mathrm{d}\phi \tag{2}$$

where $\tau = T/2$ (T is the period of the diaphragm motion); ρ_j and ρ_0 are the jet and freestream fluid densities, respectively; b is the jet orifice width; c is the chord; U_0 is the freestream velocity; and $\langle u_j(\phi)\rangle$ is the phase-averaged velocity at the jet exit plane. The velocity at the jet exit plane is measured using a miniature hot-wire sensor (5-μm tungsten), and the velocity traces are rectified when the velocity reverses its direction at midcycle. Thus, during the suction part of the cycle the velocity is inverted to reflect the correct flow direction following the procedure of Smith and Glezer.[13] The uncertainty of the velocity measured with the hot wire is ±1%.

The nominally two-dimensional flowfield associated with each of the two frequency bands is computed from a sequence of particle image velocimetry (PIV) images that are captured in the x–y plane ($z = 0$) above the suction side of the airfoil. Each PIV data set comprises three partially overlapping frames measuring 100 mm on the side where time- or phase-averaged velocity (and vorticity) distributions are computed from an ensemble of 150 image pairs. The illumination is provided by a pair of 120-mJ Nd:Yag lasers with a maximum repetition rate of 15 Hz. The laser sheet is formed using a standard optical arrangement,[14] and the images are captured using a 1008 × 1016-element charge-coupled device camera mounted on a two-axis traverse (motion resolution ±0.06 mm). The uncertainty of the velocity measured using PIV is ±3%, whereas the uncertainly in the vorticity is ±5%.

In the present work, the Reynolds number (based on the chord) is $Re_c = 3.1 \times 10^5$, and the angle of attack is $\alpha = 17.5$ deg, for which the airfoil is stalled in the absence of control. The natural shedding frequency of the separated shear layer is $F^+ = 0.7$ (Ref. 8). The jets issue from the suction side of the airfoil at $\gamma = 60$ deg, where the corresponding downstream distance from the leading edge is $x/c = 0.062$ (γ is the angle between the jets' centerline and the freestream; see Fig. 1) and their combined momentum coefficient is $C_\mu = 3.5 \times 10^{-3}$.

III. Results

Distributions of the pressure coefficient about the airfoil for $F^+ = 0.95$, 2.05, and 3.3 and $F^+ = 10$, 14.7, and 20 are shown in Figs. 2a and 2b, respectively. The pressure distributions for the (baseline) stalled flow are also shown for reference (solid line). The location of the actuator on the upper surface is marked by an arrow on each plot. Clearly, without control the flow is completely separated from the upper surface of the airfoil (as indicated by the constant pressure coefficient). Actuation at low reduced frequencies (Fig. 2a) results in a sharp suction peak around $x/c = 0.075$, which corresponds to the location of separation and the onset of the separated shear layer in the baseline flow. Whereas the streamwise decrease in static pressure for $x/c < 0.15$ appears to be independent of F^+, the degree of pressure recovery toward the trailing edge of the airfoil decreases with increasing F^+, leading to a reduction in lift and a slight increase in pressure drag. The corresponding lift and drag coefficients [as well as the lift to (pressure) drag ratios] are presented in Table 1. These data indicate that when the actuation frequency is of the same order as the shedding frequency, the lift to pressure drag ratio L/D_p decreases with increasing actuation frequency (as would be expected from the reduced receptivity of the separated shear layer to the increased actuation frequency).

The corresponding distributions of pressure coefficient for actuation at high reduced frequencies ($F^+ \geq 10$; Fig. 2b) exhibit a larger and wider suction peak than at low F^+ (Fig. 2a), and, consequently, the actuation results in a larger increment in lift [compared to

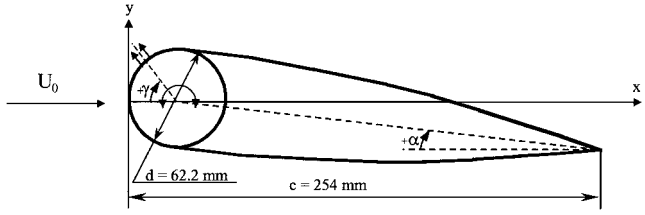

Fig. 1 Airfoil model.

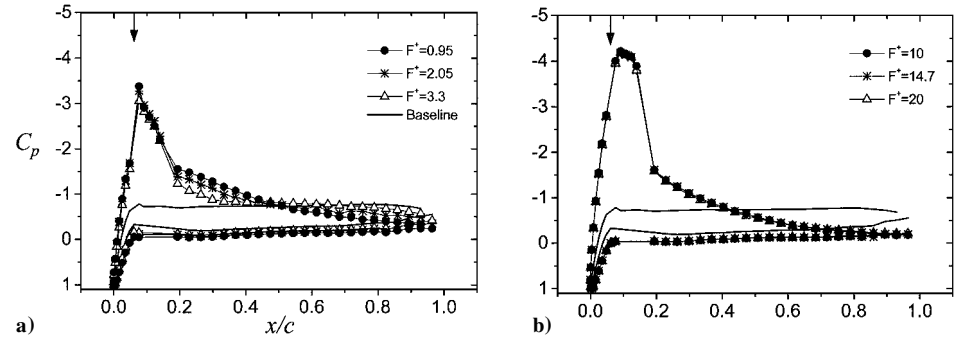

Fig. 2 Variation of the pressure coefficient with the dimensionless actuation frequency a) $F^+ \sim \mathcal{O}(1)$ and b) $F^+ \sim \mathcal{O}(10)$; $\alpha = 17.5$ deg and $\gamma = 60$ deg. (The distributions for the baseline flow are shown by a solid line.)

$F^+ \sim \mathcal{O}(1)$]. Unlike the data in Fig. 2a, the pressure recovery downstream of the suction peak in Fig. 2b appears to be essentially independent of the actuation frequency, suggesting that, for sufficiently high frequency, the details of the reattachment become frequency independent. Furthermore, as shown in Fig. 2b, the pressure difference between opposite stations on the suction and pressure surfaces of the airfoil for $x/c > 0.5$ is smaller than at corresponding streamwise stations for the low-frequency actuation, resulting in smaller contributions to the pressure drag. Similar to the data in Fig. 2a, the lift and pressure drag coefficients for the three actuation frequencies are also presented in Table 1. When the actuation frequency is more than an order of magnitude higher than the shedding frequency, L/D_p is higher than for low F^+. Furthermore, at least within the present range of high F^+, L/D_p appears to be invariant with actuation frequency, suggesting that the mechanism that leads to the suppression of separation is not associated with the stability of the separated shear layer. It is conjectured that, for a given actuation momentum coefficient, there is a domain between the two frequency ranges where the effectiveness of the actuation has a local minimum (which might be thought of as a threshold) above which the actuation effectiveness increases monotonically and reaches a fixed level where it becomes more or less frequency invariant.

Table 1 Variation of the lift and pressure drag coefficients and lift to pressure drag ratio with actuation frequency

F^+	C_L	C_{Dp}	L/D_p
0	0.34	0.34	1.0
0.95	0.80	0.30	2.67
2.05	0.77	0.31	2.48
3.30	0.73	0.31	2.35
10.00	0.91	0.28	3.25
14.70	0.90	2.28	3.22
20.00	0.90	0.28	3.22

The nominally two-dimensional flowfield associated with each of the two frequency bands is computed from a sequence of PIV images that are captured in the x–y plane ($z = 0$) above the suction side of the airfoil. Figures 3a–3g and 4a–4g show cross-stream maps of the velocity vector distributions and the discrete cross-stream velocity profile, respectively. Each of Figs. 3 and 4 includes a map of the time-averaged baseline flow (Figs. 3a and 4a) followed by pairs of phase- and time-averaged maps of the actuated flow for $F^+ = 0.95$, 3.3, and 10. Each pair includes a phase-averaged velocity field (Figs. 3b, 3d, 3f, 4b, 4d, and 4f), in which the data are taken phase locked to the actuation waveform, and a time-averaged field (Figs. 3c, 3e, 3g, 4c, 4e, and 4g). Whereas Figs. 3a–3g are the entire distributions of the velocity vectors, Figs. 4a–4g are discrete cross-stream profiles of velocity vectors at five downstream stations along the surface of the airfoil.

In the absence of control, velocity vector maps of the time-averaged baseline flow (Figs. 3a and 4a) exhibit a large recirculating flow domain with reversed flow above the surface of the airfoil. Figure 3b ($F^+ = 0.95$) clearly shows that the separating shear layer is effectively tilted toward the surface, resulting in the rollup and advection of coherent vortical structures at the actuation frequency (having a characteristic wavelength of $\sim 0.4c$). The velocity induced by these vortices is also apparent from the cross-stream profiles in Fig. 4b (note the reversed velocity induced near the wall at $x/c = 0.7$). In fact, the eddy that precedes the vortex centered at $x/c = 0.7$ is already within the wake of the airfoil. The time-averaged flow (Fig. 3c) exhibits a broad region of low-velocity near the surface, and, as shown in the corresponding plot of cross- stream velocity profiles in Fig. 4c, the time-averaged flow is actually reversed near the surface of the airfoil, indicating that the flow is not fully attached there. When the actuation frequency is increased to $F^+ = 3.3$ (Figs. 3d–3e and 4d–4e), the streamwise wavelength of the shear-layer vortices decreases to approximately $0.15c$, and the coherent structures appear to lose their phase coherence (relative to the actuation waveform) around $x/c = 0.7$, although they are clearly present in the individual snapshots. Again, the velocity vector maps

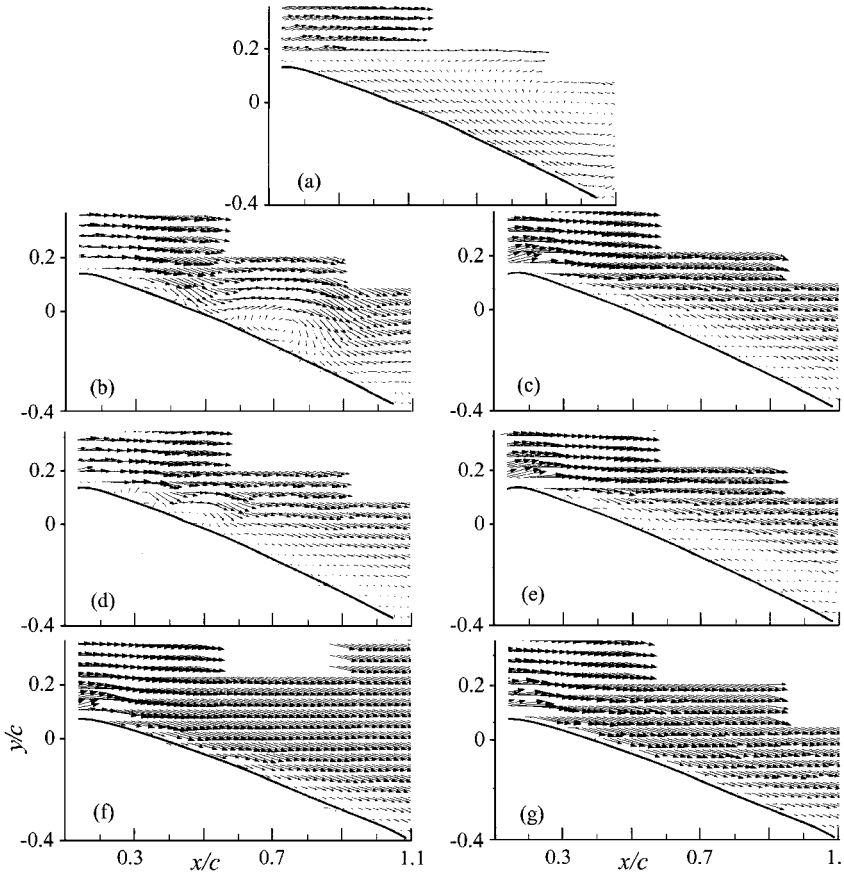

Fig. 3 Cross-stream maps of velocity vectors: a) baseline phase- and time-averaged maps pairs of the actuated flow; b, c) $F^+ = 0.95$, d, e) 3.3, and f, g) 10.

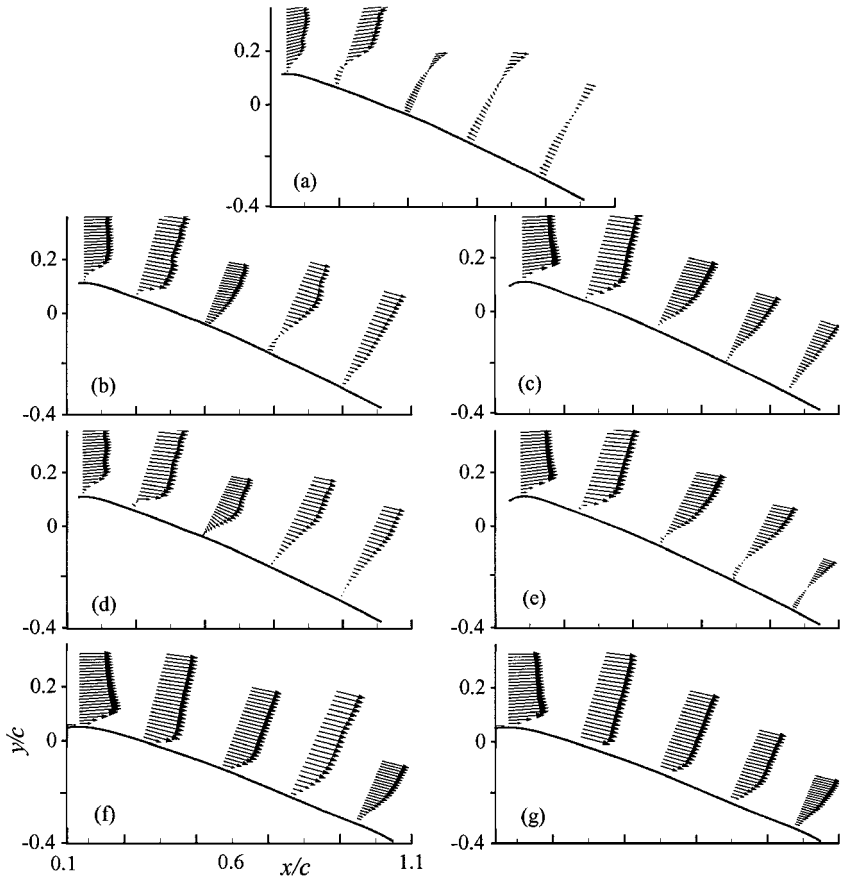

Fig. 4 Cross-stream profiles of velocity vectors (conditions as in Fig. 3).

of the time-averaged flow suggest that the flow is not fully attached, and the corresponding profiles in Fig. 4e still show a region of reversed flow near the surface that is induced by the passage of the large vortical structures.

For actuation frequency that is an order of magnitude higher than the natural baseline frequency of the separating shear layer (Figs. 3f–3g and 4f–4g) the phase coherence of the structures within the attached flow is greatly reduced compared to the lower actuation frequencies, and the boundary layer of the actuated flow appears to be fully attached over the entire length of the airfoil. In fact, the time- and phase-average vector fields are almost identical. Comparison of the time-averaged velocity profiles for the actuated flow (Figs. 4c, 4e and 4g) suggest that at low actuation frequencies the boundary layer of the mean flow is reminiscent of a thick separating boundary layer in an adverse pressure gradient, whereas for $F^+ \sim 10$ the boundary layer is significantly thinner.

Corresponding concentrations of the spanwise vorticity are computed from the velocity fields and are shown in grayscale raster images in Figs. 5a–5g. The image of the time-averaged baseline flow (Fig. 5a) shows the clockwise (CW) vorticity concentration in the separated shear layer. The vorticity field associated with the region of reversed flow on the upper surface shows a thin concentration of opposite sense [counterclockwise (CCW)] spanwise vorticity near the surface of the airfoil (indicated by the arrow). Figure 5b ($F^+ = 0.95$) shows the rollup and advection of coherent vortical structures (at the actuation frequency) in the tilted shear layer. It appears that the tilting of the shear layer results in a relatively thick CW vorticity layer adjacent to the surface of the airfoil between the actuation input and the onset of the instability that leads to the rollup of the first spanwise vortex, that is, $0.1 < x/c < 0.4$. The first spanwise eddy is centered above $x/c = 0.7$, and its nominal diameter is approximately $0.25c$. The magnitude of vorticity concentration within the preceding eddy (over the trailing edge of the airfoil) is substantially lower than in the upstream vortex because of the cross-stream spreading, ingestion of opposite sense vorticity near the surface, and perhaps partial loss of phase reference relative to the actuation signal. When the actuation frequency is increased to $F^+ = 3.3$ (Figs. 5d and 5e), the streamwise wavelength of the vortical structures decreases, and their strength (as may be measured by the concentration of spanwise vorticity) diminishes faster with streamwise distance. However, the time-averaged thickness of the vorticity layer above the surface does not appear to decrease significantly when F^+ increases from 0.95 to 3.3 (suggesting that the weakening of the spanwise vortices in the phase-averaged images is a result of loss of phase coherence). Another possible explanation is that at this frequency there is an increase in the production of negative (CCW) vorticity near the surface, which may be responsible for the enhanced weakening of the primary vortices and accelerated loss of phase coherence (beginning around $x/c = 0.8$). The data in Figs. 5b and 5d also indicate that the time-periodic formation and shedding of the vortical structures can lead to synchronous time-periodic variation in the circulation and consequently in the lift (and drag) forces as shown hereafter and is also confirmed in the numerical simulations of Donovan et al.[15] and Wu et al.[16]

When the actuation frequency is an order of magnitude higher than the natural baseline frequency of the separating shear layer (Figs. 5f and 5g), the phase coherence of the structures within the attached flow is greatly reduced, and the boundary layer of the actuated flow appears to be fully attached over the entire length of the airfoil. In fact, the time- and phase-averaged vorticity fields are almost identical.

The modification of the aerodynamic forces on the airfoil is accompanied by substantial changes in the structure of its near wake, which is investigated using x-wire anemometry. Cross-stream distributions of the time-averaged streamwise and cross-stream velocity components and of the (computed) spanwise vorticity measured at $x/c = 2$ are shown in Figs. 6a–6c, respectively (the distributions of the baseline flow are plotted using a solid line). As can be seen in Fig. 6a, when the actuation frequency is low ($F^+ = 0.95$ and 3.3), the increase in the lift to pressure drag on the airfoil is accompanied by a downward cross-stream displacement of the wake (opposite to the direction of the lift force) and a smaller velocity

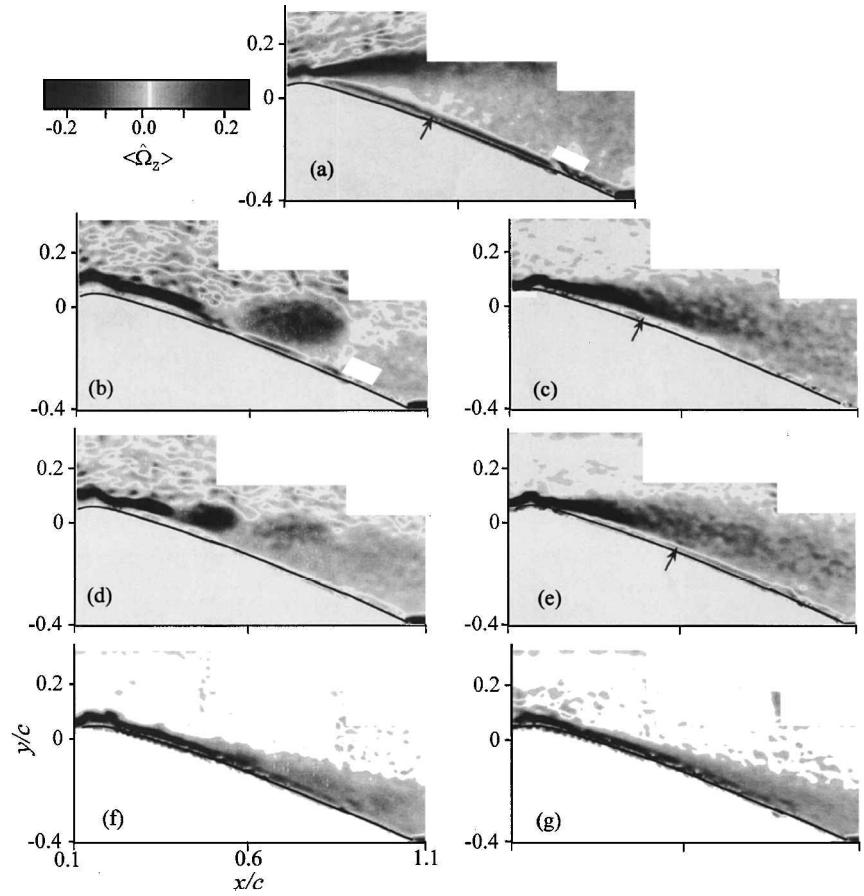

Fig. 5 Cross-stream color raster plots of vorticity concentrations (conditions as in Fig. 3).

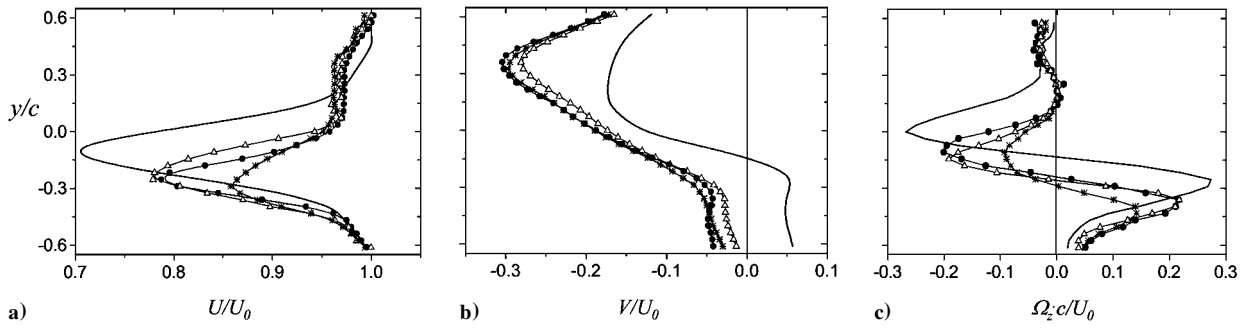

Fig. 6 Cross-stream distributions of the time-averaged a) streamwise and b) cross-stream velocity components and c) the corresponding spanwise vorticity: baseline (——), $F^+ = 0.95$ (●), $F^+ = 3.3$ (△), and $F^+ = 10$ (∗). (The distributions for the baseline flow are shown by a solid line.)

deficit. Furthermore, the cross-stream velocity in the presence of actuation has a downward offset corresponding to a downwash of the irrotational flow above the wake. The actuation also results in a smaller concentration of mean spanwise vorticity on both sides of the wake (Fig. 6c). Actuation with $F^+ = 10$ results in a considerably smaller wake deficit (Fig. 6a), indicating a further reduction in drag. At the same time, the magnitude of the (time-averaged) spanwise vorticity is also reduced, suggesting that the overall vorticity flux into the wake is reduced and also suggesting the possibility of enhanced vorticity dissipation near the trailing edge.

To further explore the difference between the two frequency regimes, the unsteadiness of the flowfield is investigated at the different actuation frequencies. Figures 7a–7d show the cross-stream distributions of the normalized phase-averaged cross-stream velocity component $\langle V(y; x = 2c)\rangle$. In each of these plots, the shaded gray area represents the cross-stream domain where the velocity deficit of the streamwise velocity is within 80% of the maximum velocity deficit (cf. Fig. 6). The time-average velocity distribution $V(y)$ is also shown in Figs. 7 for comparison. For all actuation frequencies, the cross-stream velocity above the wake (i.e., $y/d > 0$, where d is the airfoil thickness) is directed toward the wake, indicating downwash when the actuated flow is deflected toward the airfoil. At $F^+ = 0.95$ (Fig. 7a), which is of the same order as the shedding frequency ($F^+ = 0.7$), the phase-averaged distributions of the cross-stream velocity oscillate (at the actuation frequency) around the time-averaged value within the wake ($-2.5 < y/d < 0.75$) where the maximum deviation from the time-averaged velocity occurs at $y/d = -1.1$ (note that the unsteadiness of the flowfield extends beyond the edge of the measurement domain, $y/d = -2.5$). When the actuation frequency is increased to 2.05 (Fig. 7b), the deviation of the phase-averaged profiles from the corresponding time-averaged values is considerably smaller and is confined to the domain $-1.85 < y/d < -0.5$. The decrease in the fluctuations is consistent with predictions of conventional stability theory in that the amplification of the spectral component at $F^+ = 0.95$ is larger than at $F^+ = 2.05$. When the actuation frequency is increased to $F^+ = 3.3$ (Fig. 7c), the phase-averaged distributions exhibits only minimal fluctuations relative to the time-averaged profile. At

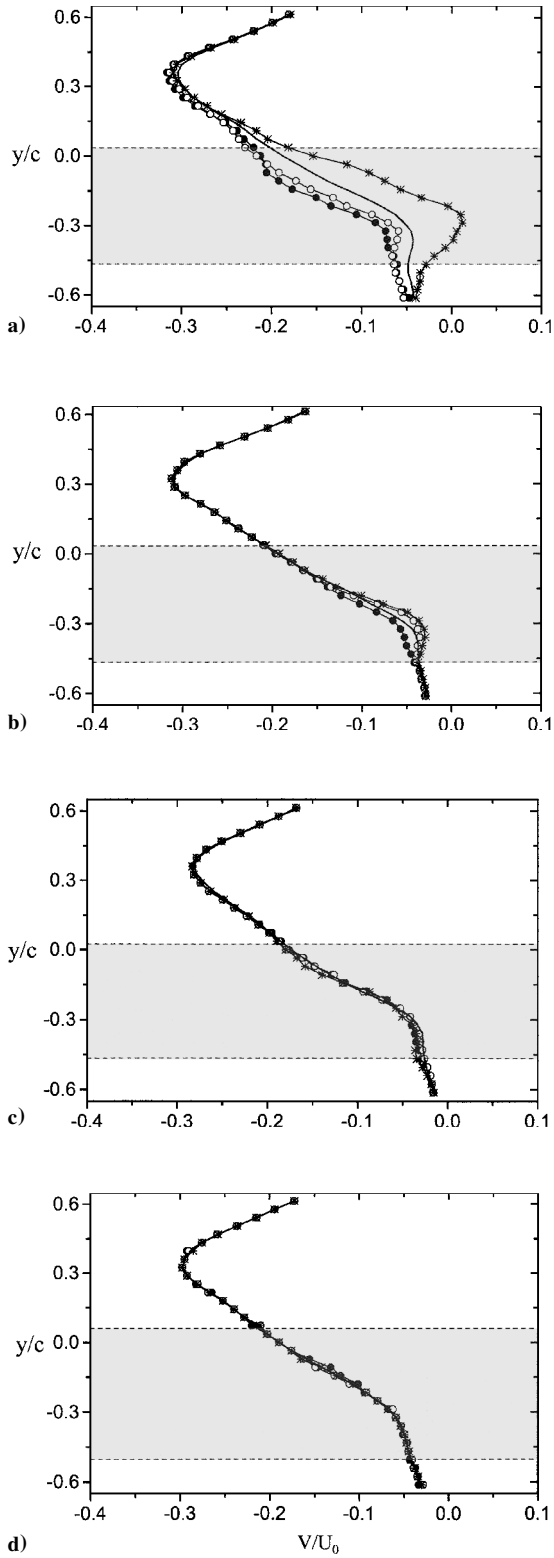

Fig. 7 Cross-stream distributions of the phase-averaged cross-stream velocity component: a) $F^+ = 0.95$, b) $F^+ = 2.05$, c) $F^+ = 3.3$, and d) $F^+ = 10$; the solid line represents the time-averaged distribution, and the symbols represent data at different phases.

$F^+ = 10$ (Fig. 7d), the phase-averaged profiles coincide with the mean distribution. As noted in connection with Fig. 3, actuation at $F^+ = 10$ leads to a relatively steady flow above the airfoil, whereas actuation at $F^+ = 3.3$ leads to the time-periodic formation of vortical structures that appear to lose their phase coherence by the time they are advected over the trailing edge. Therefore, it is not surprising that this unsteadiness is diminished by $x/c = 2$.

The time rate of change of the phase-averaged circulation, within a closed domain that includes the airfoil, is given by the vorticity flux into the wake. This flux is computed from the normalized (dimensionless) phase-averaged velocity and vorticity fields

$$\frac{\mathrm{d}\langle\hat{\Gamma}\rangle}{\mathrm{d}\hat{t}} = \int_{-\infty}^{\infty} \langle\hat{U}\rangle \cdot \langle\hat{\Omega}_z\rangle \, \mathrm{d}\hat{y} \tag{3}$$

and is shown in Figs. 8a–8d for $F^+ = 0.95$, 2.05, 3.3, and 10, respectively. (The integration does not account for contributions of the random components.) The time rate of change of the circulation may be used to infer the unsteady forces on the airfoil. To this end, the measurement station is located one chord length downstream of the trailing edge of the airfoil (x is measured from the leading

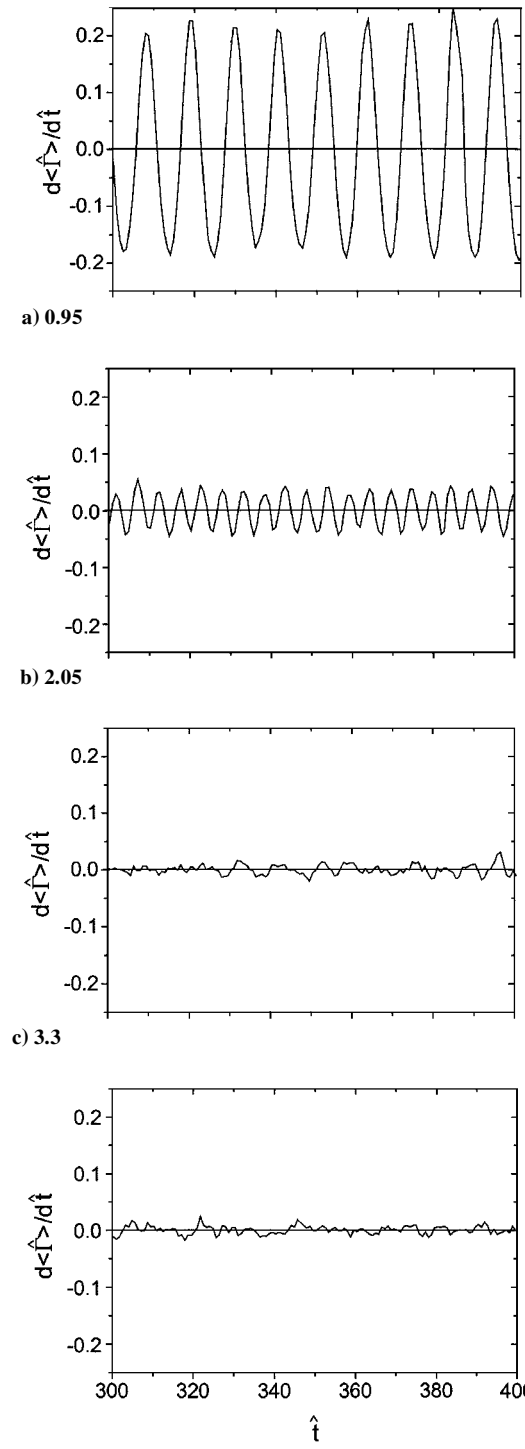

Fig. 8 Phase-locked vorticity flux as a function of normalized time at different F^+.

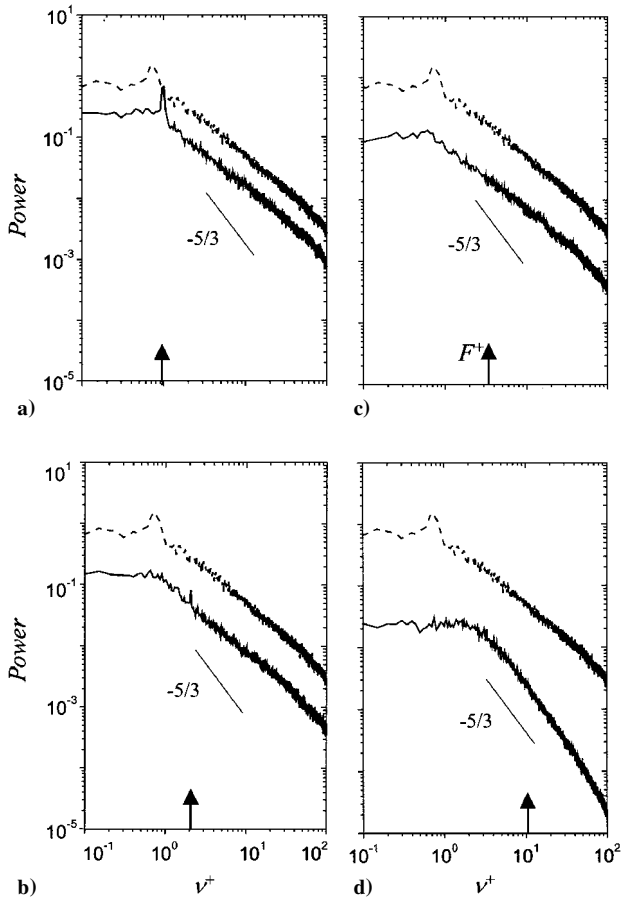

Fig. 9 Power spectra for F^+: a) 0.95, b) 2.05, c) 3.3, and d) 10; the spectrum of the baseline flow is repeated in a dash line in each frame.

edge) where the velocity fluctuations are within the calibration range of the hot-wire sensor. It is also assumed that interaction between successive vortices within this domain is minimal. In each case the time-averaged vorticity flux is nominally zero, indicating that the corresponding time-averaged circulation is invariant. However, at $F^+ = 0.95$ and 2.05 (Figs. 8a and 8b, respectively) the vorticity flux oscillates at the actuation frequency (although the amplitude of the oscillations decreases substantially between $F^+ = 0.95$ and 2.05), suggesting that the circulation (and consequently the lift force) is unsteady. When the actuation frequency is increased to $F^+ = 3.3$ and 10 (Figs. 8c and 8d), $\mathrm{d}\langle\hat{\Gamma}\rangle/\mathrm{d}\hat{t}$ exhibits virtually no oscillation at the driving frequency. Table 1 shows that, whereas the (time-averaged) lift coefficient decreases by 5% when F^+ increases from 2.05 to 3.3, at $F^+ = 10$, C_L is 20% higher than at $F^+ = 3.3$ and 12% higher then at $F^+ = 0.95$.

Power spectra of the streamwise velocity measured at $x/c = 2$ on the upper side of the airfoil wake at a cross-stream elevation, where the streamwise velocity deficit is half of the maximum deficit, are shown in Figs. 9a–9d (the spectrum of the baseline flow is reproduced using a gray line in each of Figs. 9a–9d for reference), where the dimensionless frequency is $v^+ = (f \cdot c)/U_\infty$. As is evident from the cross-stream distributions of the vorticity concentrations (Fig. 5), when the flow is actuated (and nominally attached to the upper surface of the airfoil) the cross-stream extent of the wake is reduced substantially and is accompanied by a reduction in the magnitudes of rms velocity fluctuations within the wake. At $F^+ = 0.95$ (Fig. 9) there is a strong spectral component at the actuation frequency and the entire spectrum appears to be attenuated by approximately 3.5. As F^+ is increased to 2 and 3.3, the spectral peak at the actuation frequency shifts toward the decaying part of the spectrum (it is virtually indistinguishable from the background at $F^+ = 3.3$), and the attenuation imposed by the collapse of the separated flow domain increases to 4.5 and 7, respectively. The spectrum of the actuated flow at $F^+ = 10$ (Fig. 9d) is remarkably different from the spectral distributions at the lower actuation frequencies. There is a stronger attenuation (well over an order of magnitude) at both the low and high spectral ends, and the spectrum includes a distinct inertial subrange for $v^+ > 3$ over almost two decades (which includes the actuation frequency). The reduced power at all spectral components (compared to actuation at lower F^+) indicates that the attached flow removes less energy from the uniform stream, resulting in a lower drag. Although there is no question that the flow within the wake is strongly affected by the upstream reattachment, the purpose of the spectra in Fig. 9 is to illustrate the differences between the wake flows that result from low- and high-frequency actuation.

Finally, distributions of the pressure coefficient about the airfoil at $\gamma = 10$, 25, 40, and 50 deg (Figs. 10a–10d, respectively) demonstrate that the azimuthal placement of the actuator can significantly

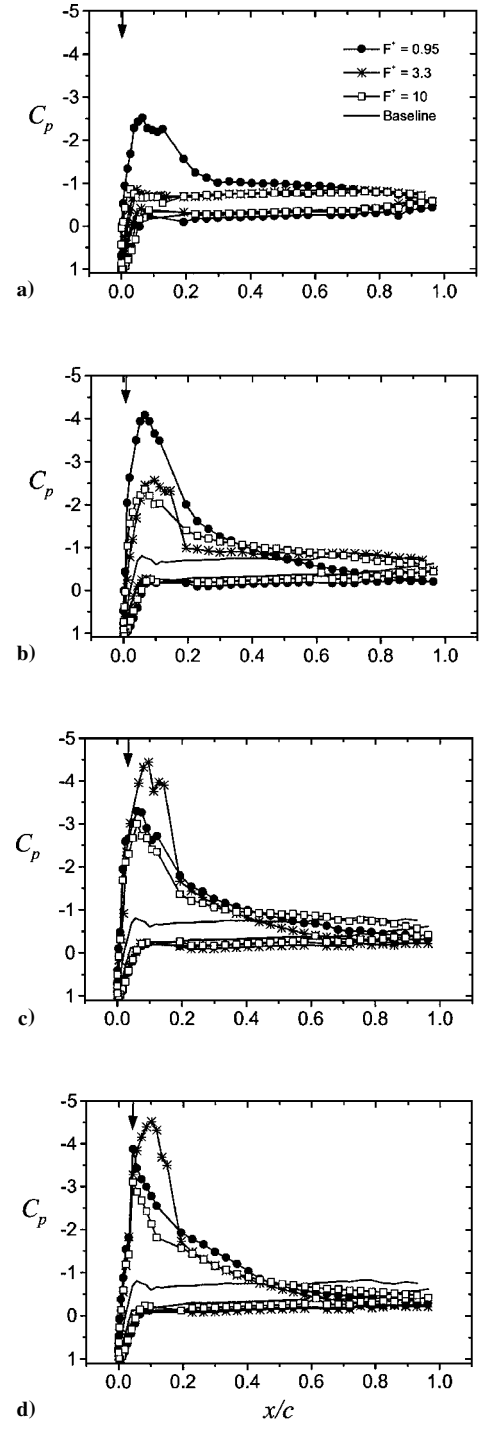

Fig. 10 Variation of the pressure coefficient with the dimensionless actuation frequency at a) $\gamma = 10$, b) 25, c) 40, and d) 50 deg; the distributions for the baseline flow are shown by solid lines.

influence the actuation effectiveness. The pressure distributions for the (baseline) stalled flow are also shown for reference. The location of the actuator for the upper surface is marked by an arrow on each plot. Actuation at $\gamma = 10$ deg ($x/c = 0.002$; Fig. 10a) with $F^+ = 3.3$ and 10 does not have a measurable effect on the flow. However, actuation at $F^+ = 0.95$ results in a suction peak around $x/c = 0.07$ that is followed by a domain ($0.08 < x/c < 0.13$) in which C_p is almost invariant, suggesting the presence of a local separation bubble. Downstream from this bubble there is short domain of pressure recovery ($0.13 < x/c < 022$) before the flow separates and reattaches again at $x/c \approx 0.75$. Actuation at $\gamma = 25$ deg ($x/c = 0.011$; Fig. 10b) with $F^+ = 3.3$ and 10 results in a partial reattachment, where the pressure distribution exhibits a small suction peak at $x/c \approx 0.08$. Whereas at $F^+ = 10$ the flow is separated (up to $x/c \approx 0.8$) downstream of the suction peak, at $F^+ = 3.3$ the flow appears to be completely attached. Note that at this jet location actuation with $F^+ = 0.95$ results in large suction peak and complete reattachment. This behavior changes for $\gamma = 40$ and 50 deg ($x/c = 0.029$ and 0.044, Figs. 10c and 10d, respectively), where actuation at high frequency ($F^+ = 10$) results in a larger and wider suction peak than at low F^+. Furthermore, similar to the pressure distributions at $\gamma = 60$ deg (Figs. 2a and 2b), the pressure difference across the airfoil for $x/c > 0.2$ is smaller than at corresponding streamwise stations for the low-frequency actuation, resulting in smaller contributions to the pressure drag.

Other parameters that directly influence the degree of control effectiveness of the present actuators (e.g., the actuation momentum coefficient, airfoil angle of attack, Reynolds number, etc.) were discussed previously in some detail (Smith et al.[8] and Amitay et al.[9,10,12]). Amitay et al.[12] showed that the effect of the present actuation applied to the present airfoil is invariant up to $Re_c = 7.5 \times 10^5$. Furthermore, Amitay et al.[9] showed that the actuation is effective even when the boundary layer is artificially tripped. In their experiments, a two-dimensional cylinder was specifically selected for the purpose of this demonstration because the base flow is extensively documented and is inherently separated. Because the leading edge of the present airfoil comprises a circular cylinder, it is believe that the earlier results apply for the present airfoil. Moreover, the work of Seifert and Pack[17] demonstrated that the effectiveness of separation control at low actuation frequencies is virtually invariant with respect to the Reynolds number up to $Re_c = 30 \times 10^6$.

IV. Conclusions

Wind-tunnel experiments are conducted to investigate the effect of the actuation frequency on the coupling between the synthetic jets and the crossflow. The actuation frequency is varied between the unstable frequency of separating shear layer and operating frequencies that are at least an order on magnitude higher ($0.95 < F^+ < 20$). The experiments are conducted at $Re_c = 3.1 \times 10^5$, and, in the absence of control, the flow separates at angles of attack exceeding 5 deg. Flow reattachment leads to an increase in the lift to pressure drag ratio for all actuation frequencies. However, actuating at $F^+ \sim \mathcal{O}(10)$ results in a larger increase in the lift to pressure drag ratio than actuating at $F^+ \sim \mathcal{O}(1)$.

The present data show that, depending on the actuation frequency, the lift to pressure drag ratio has two distinct regimes. In the first regime, the actuation frequency is of the same order of the shedding frequency ($F^+ < 4$), and L/D_p decreases with the actuation frequency. In the second regime, the actuation frequency is at least an order of magnitude higher than the shedding frequency, for example, $F^+ \geq 10$. Within this regime, L/D_p is nominally 27% higher than the level within the low-frequency domain and is virtually invariant with the actuation frequency. Moreover, velocity measurements in the cross-stream plane above the airfoil clearly indicate that at low actuation frequencies the separating shear layer is tilted toward the surface (similar to a Coanda effect), and there is substantial recovery of lift and reduction of the pressure drag.

The time rate of change of the phase-averaged circulation (given by the vorticity flux into the wake of the airfoil) is computed from the phase-averaged velocity and vorticity fields. At actuation frequencies that are of the same order as the unstable shedding frequency of the separated shear layer ($F^+ = 0.95$ and 2.05) the vorticity flux oscillates at the actuation frequency, suggesting that the circulation (and consequently the lift force) is unsteady. Similar findings from earlier numerical simulations indicated variations in lift that are as high as 20%. At higher actuation frequencies ($F^+ = 3.3$ and 10), the normalized phase-averaged vorticity flux $\mathrm{d}\langle\hat{\Gamma}\rangle/\mathrm{d}\hat{t}$ exhibits virtually no oscillation at the driving frequency and, therefore, indicates relatively steady aerodynamic forces.

Spectral measurements in the wake of the airfoil indicate that there is a substantial difference in the nature of flow reattachment on the top surface of the airfoil at low and high actuation frequency domains. It is remarkable that actuation at high frequency leads not only to the appearance of a featureless spectrum, but also to the emergence of a spectral band having a $-\frac{5}{3}$ slope, indicating enhanced dissipation.

Acknowledgments

This work was supported by the U.S. Air Force Office of Scientific Research (monitored by T. Beutner). The technical support of Boeing's Phantom Works in St. Louis in the fabrication and maintenance of the fairing hardware is gratefully acknowledged. The authors would also like to thank M. Lal and E. Chatlynne at the Georgia Institute of Technology for their assistance in the acquisition of the particle image velocimetry data.

References

[1] Chang, P., *Control of Flow Separation*, Hemisphere, New York, 1976.

[2] Attinello, J. S., "Design and Engineering Features of Flap Blowing Installations," *Boundary Layer and Control*, Vol. 1, 1961, pp. 463–515.

[3] Seifert, A., Darabi, A., and Wygnanski, I., "Delay of Airfoil Stall by Periodic Excitation," *Journal of Aircraft*, Vol. 33, No. 4, 1996, pp. 691–698.

[4] Urzynicok, F., and Fernoholz, H. H., "Separation Control on an Airfoil Under Post-Stall Conditions by Mechanical Excitation," *Proceedings of the IUTAM Symposium: Mechanics of Passive and Active Flow Control*, International Union of Theoretical and Applied Mechanics, 1998, pp. 249–254.

[5] Modi, V. J., Munshi, S. R., and Yokomizo, T., "Moving Surface Boundary Layer Control as Applied to Slender and Bluff Bodies," *Proceedings of the IUTAM Symposium: Mechanics of Passive and Active Flow Control*, International Union of Theoretical and Applied Mechanics, 1998, pp. 285–290.

[6] Ahuja, K. K., and Burrin, R. H., "Control of Flow Separation by Sound," AIAA Paper 84-2298, 1984.

[7] Chang, R. C., Hsiao, F.-B., and Shyu, R.-N., "Forcing Level Effects of Internal Acoustic Excitation on the Improvement of Airfoil Performance," *Journal of Aircraft*, Vol. 29, No. 5, 1992, pp. 823–829.

[8] Smith, D. R., Amitay, M., Kibens, K., Parekh, D. E., and Glezer, A., "Modification of Lifting Body Aerodynamics Using Synthetic Jet Actuators," AIAA Paper 98-0209, 1998.

[9] Amitay, M., Smith, B. L., and Glezer, A., "Aerodynamic Flow Control Using Synthetic Jet Technology," AIAA Paper 98-0208, 1998.

[10] Amitay, M., Kibens, V., Parekh, D. E., and Glezer, A., "Flow Reattachment Dynamics over a Thick Airfoil Controlled by Synthetic Jet Actuators," AIAA Paper 99-1001, 1999.

[11] Erk, P. P., "Separation Control on a Post-Stall Airfoil Using Acoustically Generated Perturbations," Ph.D. Dissertation, Verkehrswesen und Angewandte Mechanik, Technische Univ. Berlin, Berlin, 1997.

[12] Amitay, M., Smith, D. R., Kibens, V., Parekh, D. E., and Glezer, A., "Modification of the Aerodynamics Characteristics of an Unconventional Airfoil Using Synthetic Jet Actuators," *AIAA Journal*, Vol. 39, No. 3, 2001, pp. 361–370.

[13] Smith, B. L., and Glezer, A., "The Formation and Evolution of Synthetic Jets," *Physics of Fluids*, Vol. 10, No. 9, 1998, pp. 2281–2297.

[14] Raffel, M., Willert, C., and Kompenhans, J., *Particle Image Velocimetry*, Springer-Verlag, Berlin, 1998, pp. 33–38.

[15] Donovan, J. F., Kral, L. D., and Cary, A. W., "Active Flow Control Applied to an Airfoil," AIAA Paper 98-0210, 1998.

[16] Wu, J.-Z., Lu, X.-Y., Denny, A. G., Fan, M., and Wu, J.-M., "Post-Stall Control on an Airfoil by Local Unsteady Forcing," *Journal of Fluid Mechanics*, Vol. 371, 1998, pp. 21–58.

[17] Seifert, A., and Pack, L. G., "Oscillatory Control of Separation at High Reynolds Numbers," *AIAA Journal*, Vol. 37, No. 9, 2001, pp. 1062–1071.

J. C. Hermanson
Associate Editor